Chapter 8

ULTIMATE BEARING CAPACITY OF STRIP FOOTING ON UNSATURATED SANDY SOIL UNDER COMBINED LOAD

8.1 INTRODUCTION

In the preceding chapter, the behaviour of strip footing resting on unsaturated sandy soil was demonstrated after applying the essential modifications on the finite element upper bound limit analysis. The modification was carried out to integrate the matric suction as a stress state variable within the partially saturated zone. The effect of unsaturated soil property functions, water-table positions, and seasonal changes can duly be assessed through the modified UB-FELA technique. As part of the analysis, the concentric vertical load was applied to the strip footing. However, the strip footings which support super-structure like retaining walls, abutments, stanchions, and portal-framed buildings are often subjected to either oblique and/or eccentric load. The effects of combined loading on the bearing capacity of strip footing are addressed by a few researchers through experimental analysis (Gottardi and Butterfield, 1993; Patra et al., 2012; Gupta and Mital, 2022), analytical methods (Meyerhof, 1953, 1963; Hansen, 1970; Prakash and Saran, 1971; Vesic, 1975; Fedorovskii, 2003; Ganesh et al., 2017; Viladkar et al., 2013), and numerical techniques (Hjiaj et al., 2004; Saran and Agarwal, 1991; Zdravkovic et al., 2002; Massih et al., 2005; Loukidis et al., 2008; Zhan, 2011; Krabbenhoft et al., 2012, 2014; Ornek, 2014; Tang et al., 2015; Yahia-Cherif et al., 2017; Zheng et al., 2019). These studies qualitatively and quantitatively described the impact of the loading position and its orientation on the ultimate bearing capacity and the developed failure mechanisms. However, these studies were primarily conducted by considering the two extreme saturation states of the soil (i.e., S=0 and S=1). Considering

the effect of the vadose zone, a few studies were also conducted to determine the ultimate bearing capacity of strip footing under the action of inclined loading (Jin et al., 2021) as well as combined loadings (Fathipour et al., 2022, 2023). Idealizing the linear forms of matric suction (homogenous variation and linearly increasing variation) above the groundwater table, Jin et al. (2021) investigated the effect of inclined load on the strip foundations with the help of the rigid block upper bound limit theorem in association with the improved radial movement optimization algorithm. With the aid of lower bound limit analysis, the combined effects of inclined and eccentric loading on the bearing capacity of strip footing were rigorously examined for the steady state (Fathipour et al., 2022) and the transient state (Fathipour et al., 2023). However, no finite element upper bound study seems to exist in the available literature for determining the UBC of strip footing placed over unsaturated soils by considering the effect of different loading arrangements and nonlinear matric suction profiles. The present chapter investigates the ultimate bearing capacity of strip foundations that are rested on variably saturated soils and subjected to eccentric and inclined loadings. This investigation is carried out by employing the SSCC-based UB-FELA formulations, as mentioned in the previous chapter. An extensive parametric study is conducted, and the bearing capacity charts are prepared by varying the groundwater table position, flow conditions, hydromechanical properties, and loading position and orientation.

8.2 PROBLEM STATEMENT AND DOMAIN

A rough and rigid strip footing of width B (1m), as shown in Figure 8.1a, is rested over homogenous and isotropic sandy soil. The ground surface is considered to be horizontal and surcharge-free. The groundwater table is located at a depth of h_w below the ground surface. The loading is applied at a distance of e from the central axis of the footing and at an angle (counter-clockwise is taken to be positive) of β, measured

from the vertical axis. The load is placed within a certain zone (e/B < 1/3) so that no tensile stress is being developed beneath the footing. In this context, it is required to mention that if the load is inclined towards the center line of the footing it is

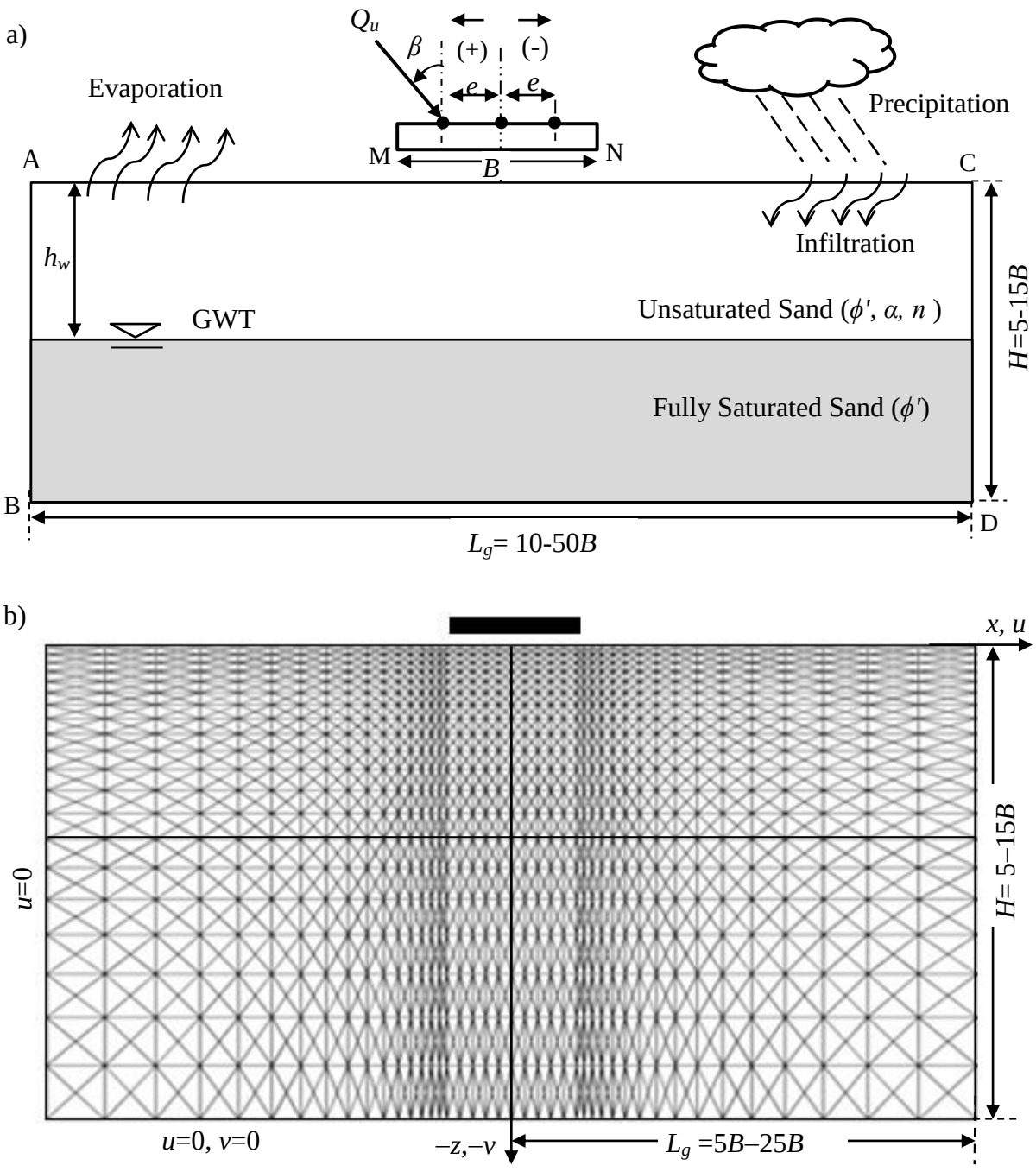

Figure 8.1 a) Domain used for strip footing resting on sandy soil; and b) mesh used for analysis.

termed as reinforced condition, whereas, if the load is inclined away from the center line of the footing it is referred to as a partially compensated condition (Perloff and Barron, 1976). This study intends to rigorously verify the load-carrying capacity of strip footing rested over partially saturated sands and subjected to

eccentric and oblique loading by varying the eccentricity (e), load inclination (β), soil parameters (ϕ, α, n), and location of the groundwater table (h_w).

Figure 8.1 represents the domain and mesh used in the present analysis. The extent of the domain is chosen in such a way that the nodal velocity patterns are well contained within the domain and the solutions remain unaltered by any further extension of the domain size. The vertical and the horizontal extent of the domain are considered as 5-15B and 10-50B, respectively. Along the sides AB and CD, the horizontal movement is restrained and along the bottom (BD), both vertical and horizontal movements are taken to be zero. There are no velocity constraints along the ground surface AM and NC.

8.3 ANALYSIS

In the preceding chapter, the modifications in the upper-bound formulations were carried out considering the following two aspects: (a) incorporation of the modified (suction stress-based) effective stress equations, and (b) inclusion of the suction stress characteristics curve. The SSCC is intrinsically formed by combining the van-Genuchten SWRC model, Gardner's HCF, Darcy's law, continuity equation, and closed-form suction stress formulation. The structure of the UB-FELA technique adopted in this chapter is the same as the previous one. Nonetheless, following Ukritchon et. al. (1998), a slight adjustment is required to be made in order to amend the effect of inclined and eccentric loading. In contrast to the vertical, concentric loading the combined loading induces direct sliding along the interface and separation of the

footing base from the underlying soil. The permitted velocity discontinuity across the soil-footing interface enables the movement of the rigid footing independently from the underlying soil. The motion of the rigid footing is fully described by the following three degrees of freedom mentioned at the center of the footing base: horizontal velocity (u_{cg}), vertical velocity (v_{cg}), and angular velocity (w_{cg}). Figure 8.2 presents a footing that is aligned at an angle of Ω with the horizontal axis. The footing is subjected to an inclined and eccentric load of magnitude, Q. The inclination angle (angle between the load direction and perpendicular axis of the footing) and the eccentricity are designated with the symbols, β and e, respectively. The rate of work done by the traction force (P_{ext}^{tr}) is evaluated by multiplying the applied load, Q, with the velocity component along the load direction.

$$P_{ext}^{tr} = Q(\sin(\beta+\Omega)u_B - \cos(\beta+\Omega)v_B - e\cos\beta w_{cg}) \tag{8.1}$$

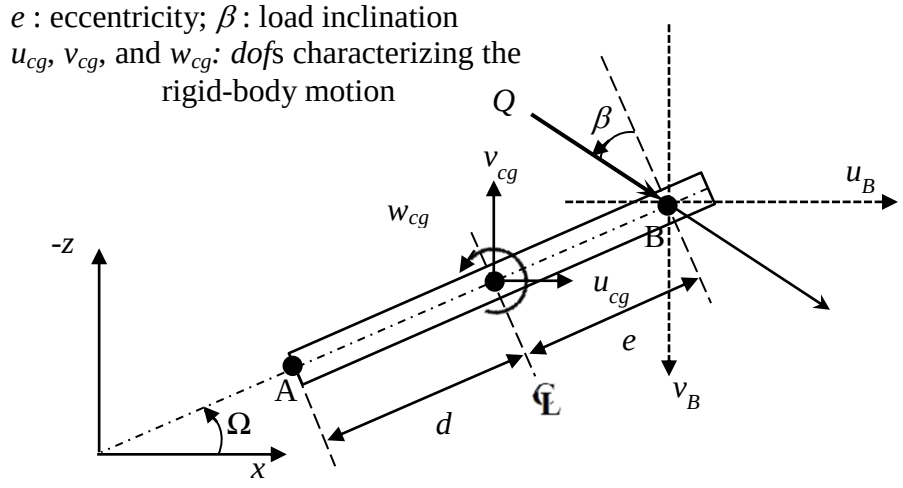

Figure 8.2 Rigid footing subjected to inclined and eccentric load

The velocities vary linearly along the footing. The velocities at any node can be expressed as follows:

At loading point (B): $u_B = u_{cg} - w_{cg} e\sin\Omega$ (8.2a)

$$v_B = v_{cg} + w_{cg} e \sin \Omega \tag{8.2b}$$

At any arbitrary point (A): $u_A = u_{cg} - w_{cg} d \sin \Omega$ (8.3a)

$$v_A = v_{cg} + w_{cg} d \sin \Omega \tag{8.3b}$$

where, (i) (u_A, v_A) and (u_B, v_B) are the horizontal and vertical velocities at points A and B, respectively, and (ii) d is the distance from the center of the footing to point A.

Substituting Equations (8.2a) and (8.2b) in Equation (8.1), the expression of power dissipation due to traction becomes:

$$P_{ext}^{tr} = Q(R_1 u_{cg} - R_2 v_{cg} - R_3 w_{cg}) = Q d_B \tag{8.4}$$

where, $R_1 = \sin(\beta + \Omega)$; $R_2 = \cos(\beta + \Omega)$;

$$R_3 = e(\sin \Omega \sin(\beta + \Omega) + \cos(\beta + \Omega) \sin \Omega + \cos \beta)$$

According to the principle of virtual work equation: $P_{ext}^{tr} + \int \gamma v dA = P_{int}$ (8.5)

The UBC (Q_u) is obtained by minimizing the following objective function with an additional constraint mentioned in Equation (8.8).

Objective Function: $Q_u = Min.\ Q = Min.\ P_{ext}^{tr} = Min.\ \left(P_{int} - \int \gamma v dA\right) / d_B$ (8.6)

$$= \left(\sum_{e=1}^{E} P_{2e} + \sum_{d=1}^{D_c} P_{3d} - \sum_{e=1}^{E} P_{1e} \right) / d_B \tag{8.7}$$

Additional constraint: $R_1 u_{cg} - R_2 v_{cg} - R_3 w_{cg} = d_B$ (8.8)

Physically, Equation (8.8) imposes a restriction of virtual displacement of d_B unit at point B along the loading direction. In the previous chapter, the normal velocity of all the nodes along the footing base was the same (i.e. v_n). The numerical simulations are performed by setting the absolute values of v_n and d_B to unity. Apart from the additional constraint (Equation (8.8)) of d_B displacement at point B, the effect of combined loading is realized by relating the nodal velocities of the footing base to three unknown velocities at the center (u_{cg}, v_{cg}, and w_{cg}). That

is how the treatment of vertical and concentric load differs fundamentally in its approach compared to the handling of combined loading.

8.4 RESULTS AND DISCUSSION

By using the UB-FELA analysis, the bearing capacities are determined for various combined set of parameters, as mentioned below:

Drained frictional angle: $\phi^{'} = 35°, 45°$

Load Eccentricity: $e/B = 0, 0.25, –0.25$

Load Inclination: $\beta = 0°, 10°, 20°,$

vG parameters: α =0.1, 0.3, 0.5, 0.7, and 0.9 kPa^{-1} , n =2, 3, 4, and 5

Water Table Position: h_w= 0, 1, 2, 3, 4, 5, and 6 m.

A total number of 2432 of simulations are run for this study and the obtained solutions are reported in terms of the bearing capacities.

8.4.1 Bearing capacity charts

Figures 8.3–8.8 depict the variations of the UBC with respect to the water table fluctuation for various loading conditions and hydromechanical parameters; Figures 8.3–8.5 pertain to $\phi' = 35°$ and Figures 8.6–8.8 conforms to $\phi' = 45°$. Moreover, (a) Figures 8.3 and 8.6 correspond to e =0, (b) Figures 8.4 and 8.7 are related to e = 0.25, and (c) Figures 8.5 and 8.8 are connected to e = –0.25. Each of these figures is drawn for various α, n, and β values. The following observations and interpretations are made from this study.

a) The UBC of unsaturated soil (h_w>0) is always greater than the UBC of fully saturated soil (h_w = 0). This can be attributed to the fact that the presence of

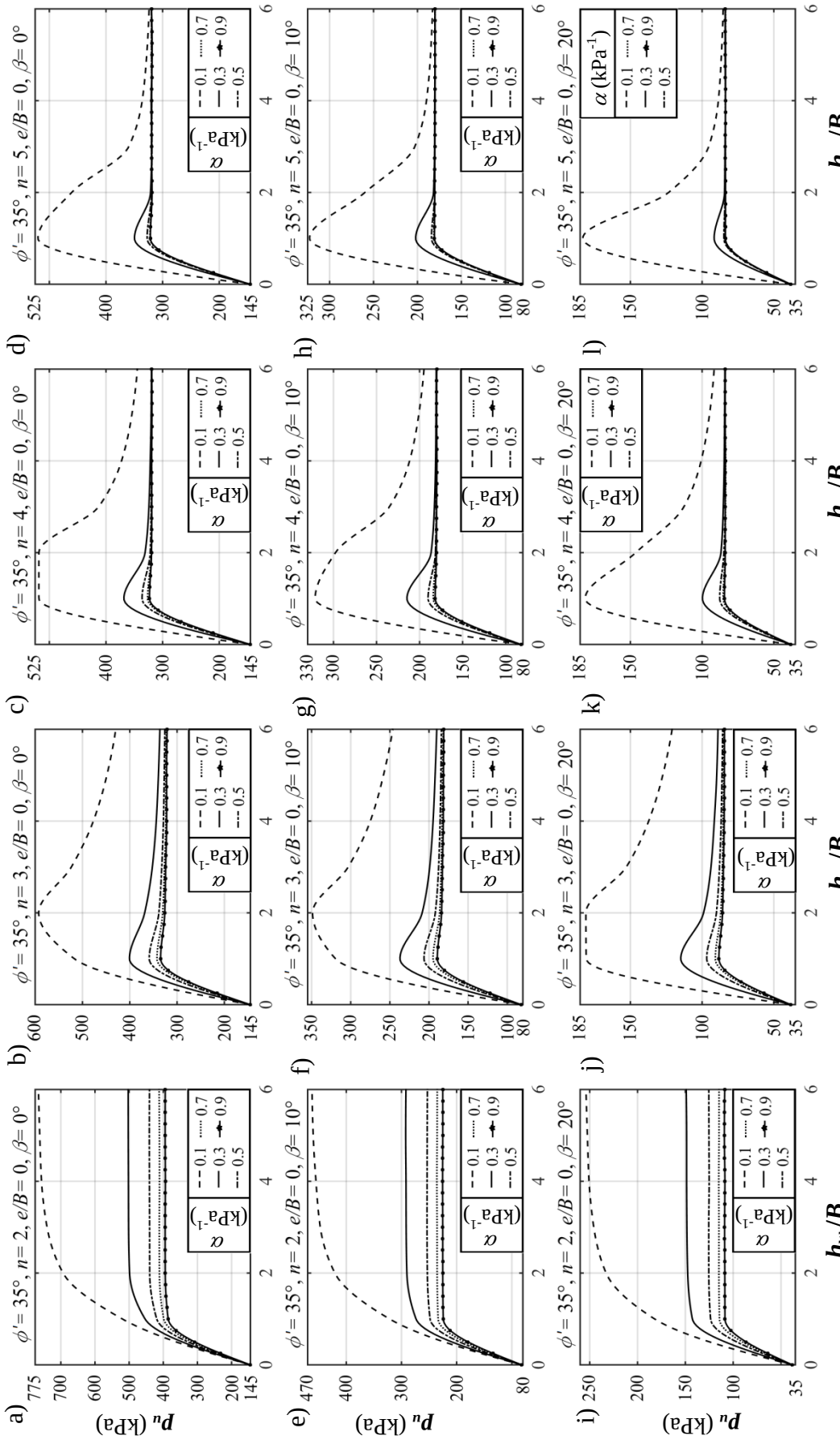

Figure 8.3 The variation of UBC (p_u) with respect to GWT for sands with ϕ' = 35°, e/B =0, and subjected to three β, namely, (a-d) β=0°; (e-h) β=10°; and (i-l) β=20°; and corresponding to four values of n, namely, (a,e,i) n =2; (b,f,j) n =3; (c,g,k) n =4; and (d,h,l) n =5.

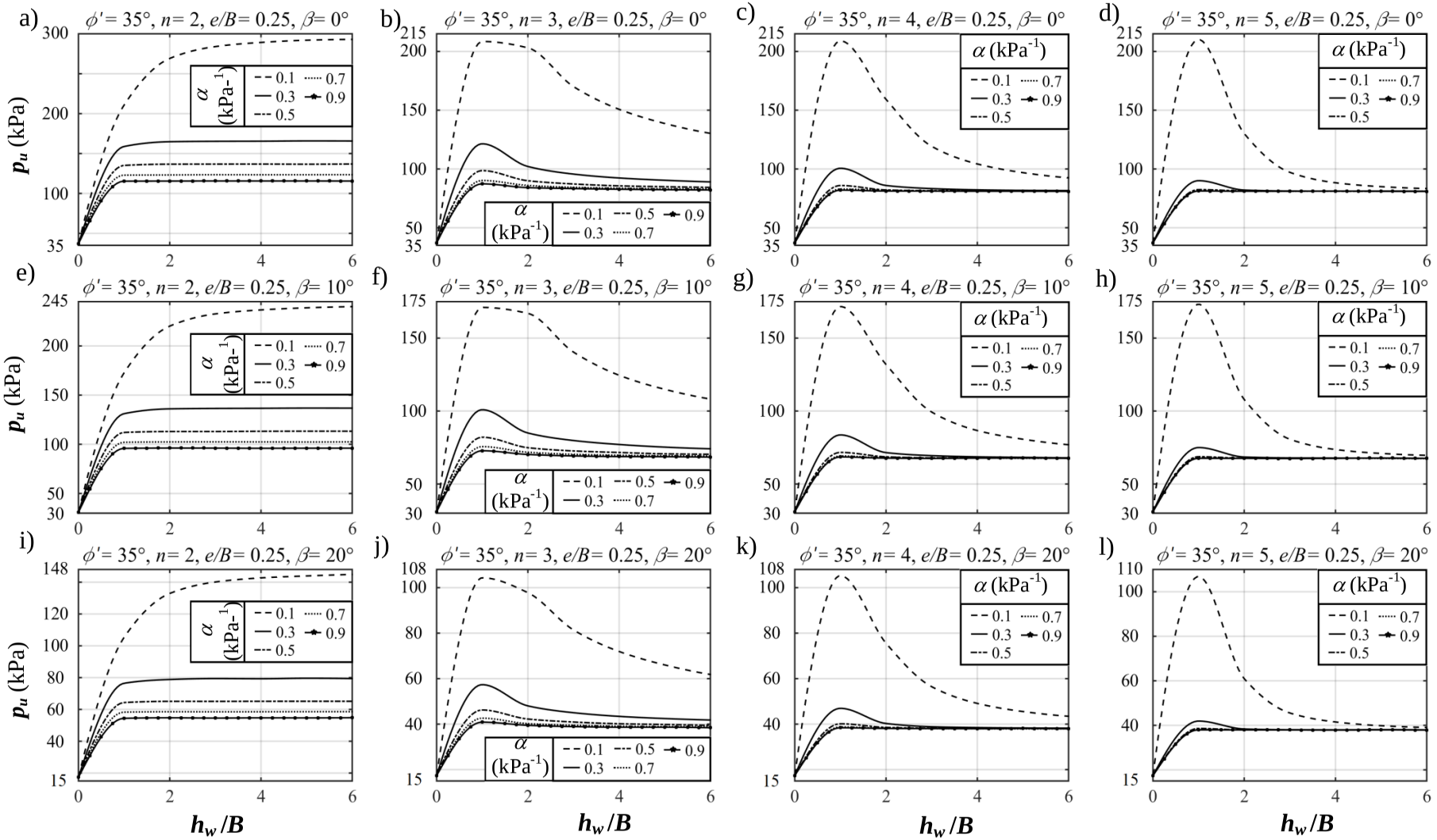

Figure 8.4 The variation of UBC (p_u) with respect to GWT for sands with ϕ' = 35°, *e/B* =0.25, and subjected to three β, namely, (a-d) β=0°; (e-h) β=10°; and (i-l) β=20°; and corresponding to four values of *n*, namely, (a,e,i) *n* =2; (b,f,j) *n* =3; (c,g,k) *n* =4; and (d,h,l) *n* =5.

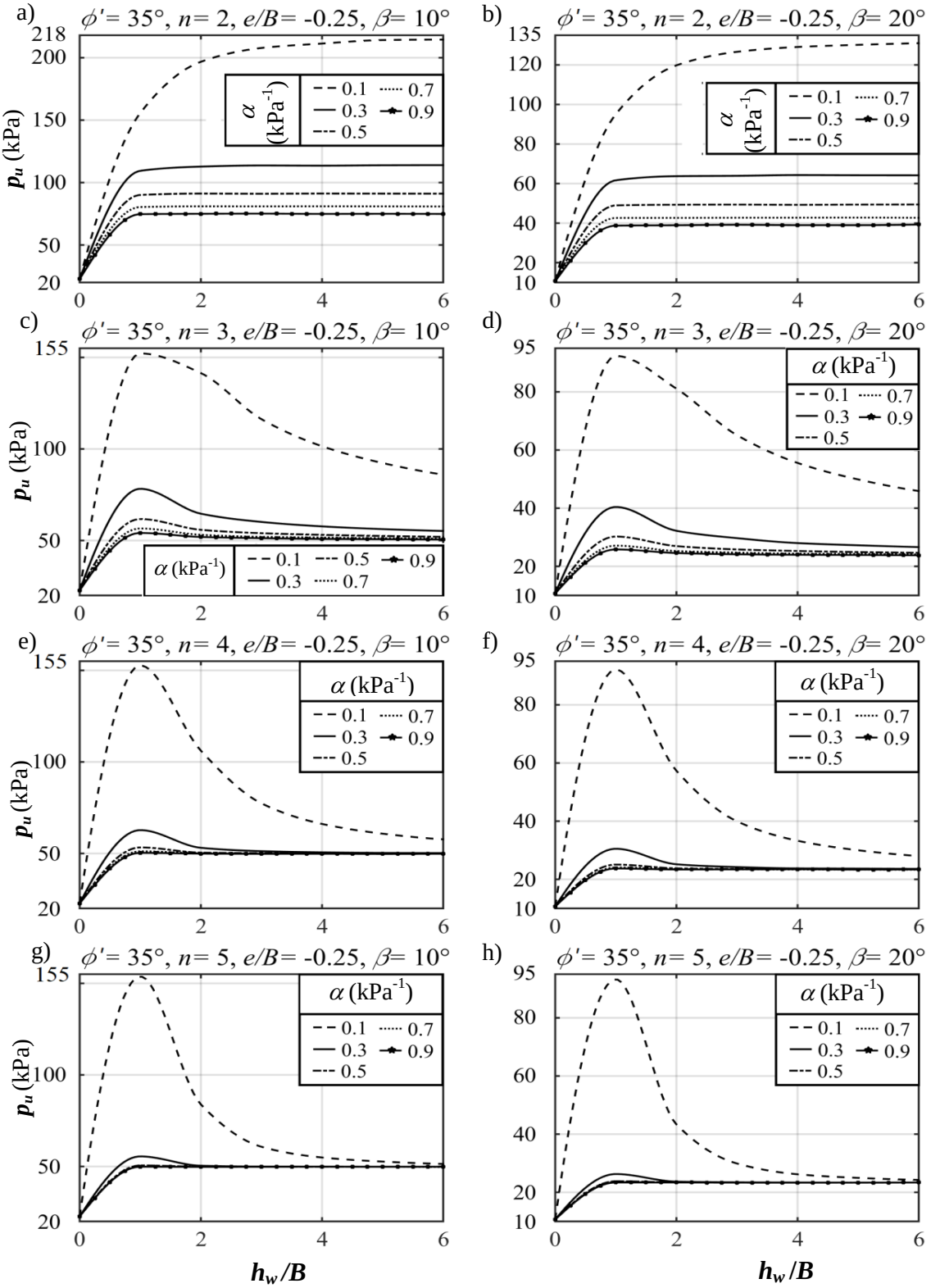

Figure 8.5 The variation of UBC (p_u) with respect to GWT for sands with ϕ' = 35°, *e/B* = – 0.25, and subjected to two β, namely, (a,c,e,g) β=10°; (b, d, f, h) β=20°; and corresponding to four values of *n*, namely, (a,b) *n* =2; (c,d) *n* =3; (e,f) *n* =4; and (g,h) *n* =5.

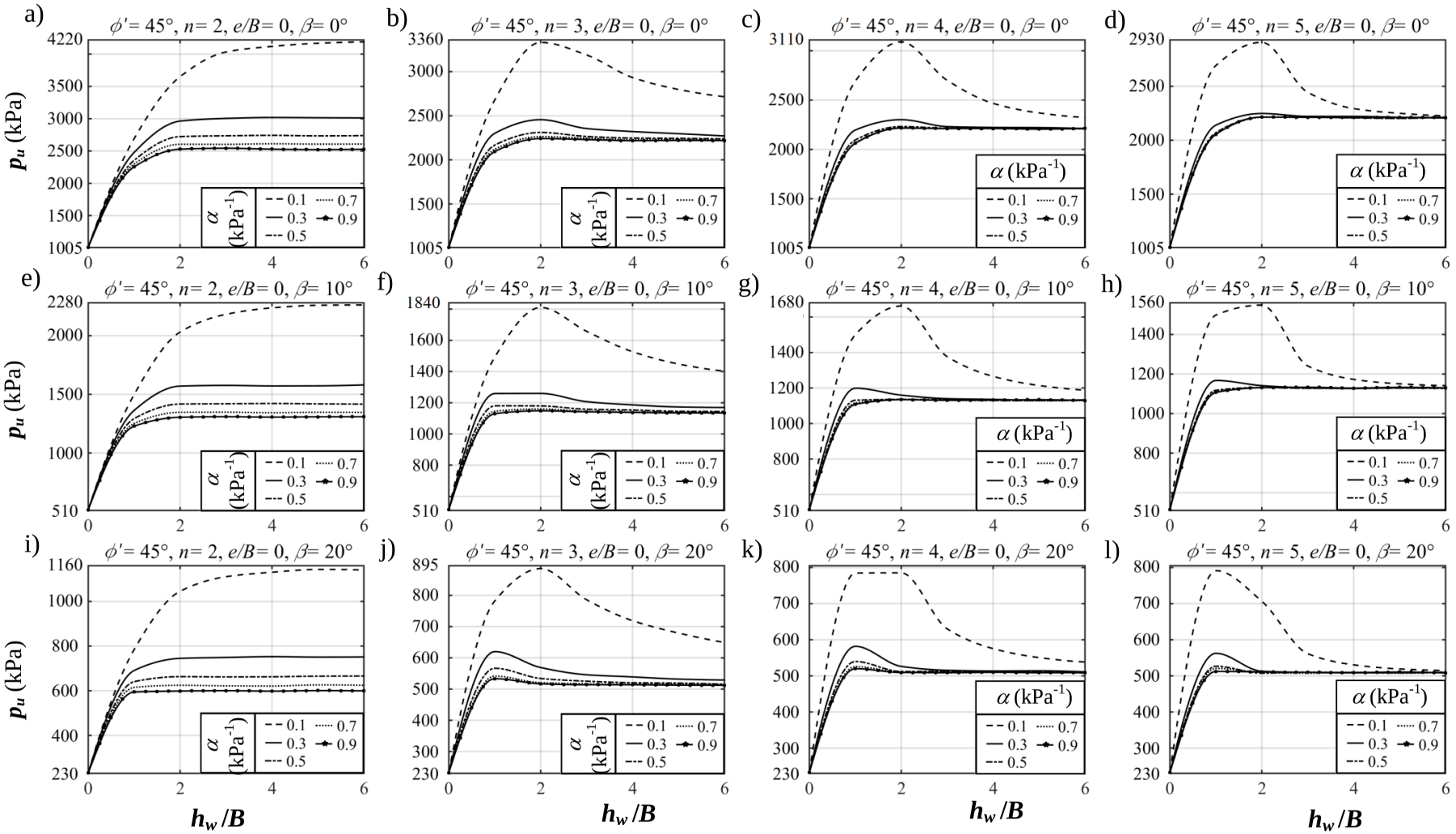

Figure 8.6 The variation of UBC (p_u) with respect to GWT for sands with ϕ' = 45°, e/B =0, and subjected to three β, namely, (a-d) β=0°; (e-h) β=10°; and (i-l) β=20°; and corresponding to four values of n, namely, (a,e,i) n =2; (b,f,j) n =3; (c,g,k) n =4; and (d,h,l) n =5.

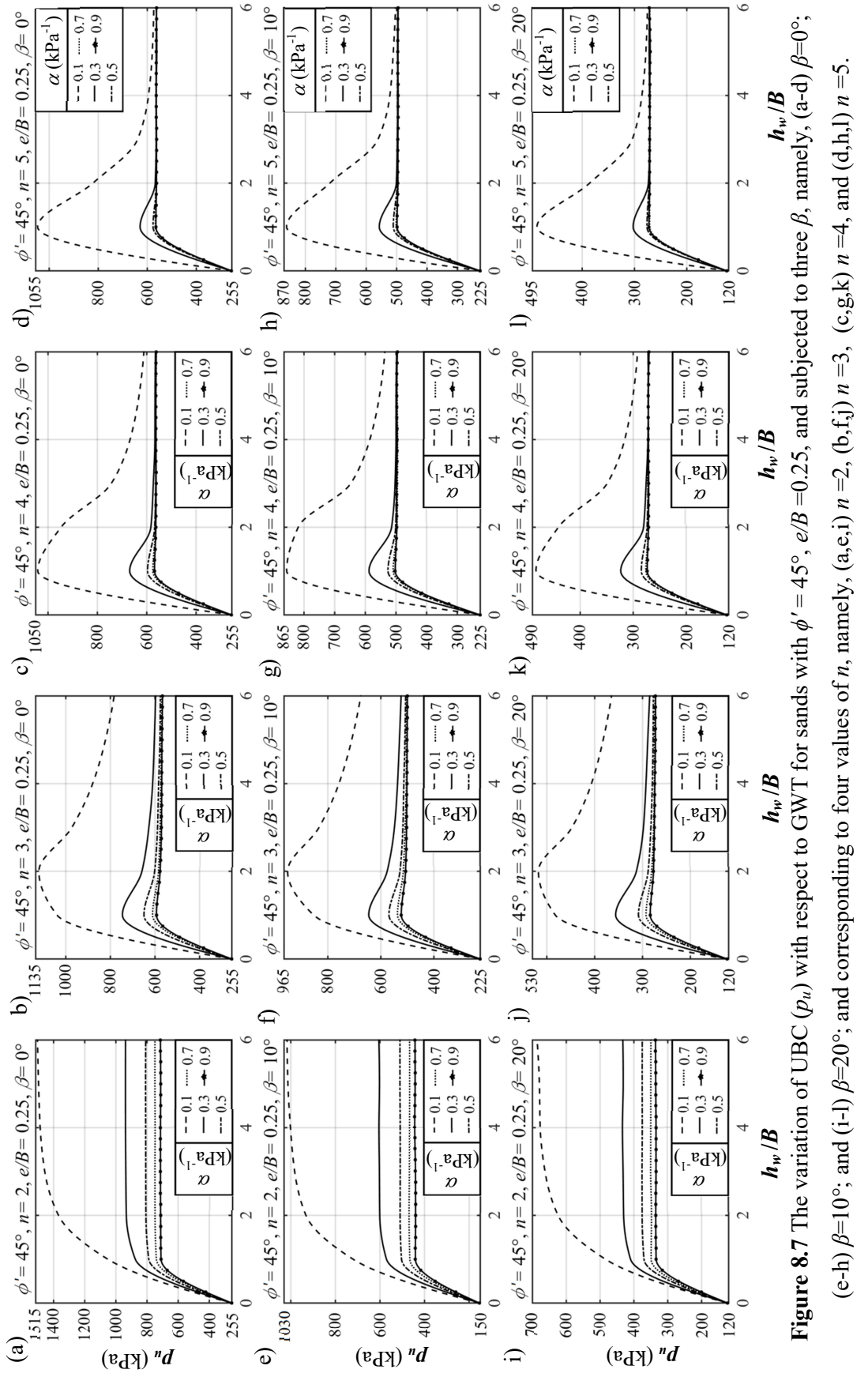

Figure 8.7 The variation of UBC (p_u) with respect to GWT for sands with ϕ' = 45°, e/B =0.25, and subjected to three β, namely, (a-d) β=0°; (e-h) β=10°; and (i-l) β=20°; and corresponding to four values of n, namely, (a,e,i) n =2, (b,f,j) n =3, (c,g,k) n =4, and (d,h,l) n =5.

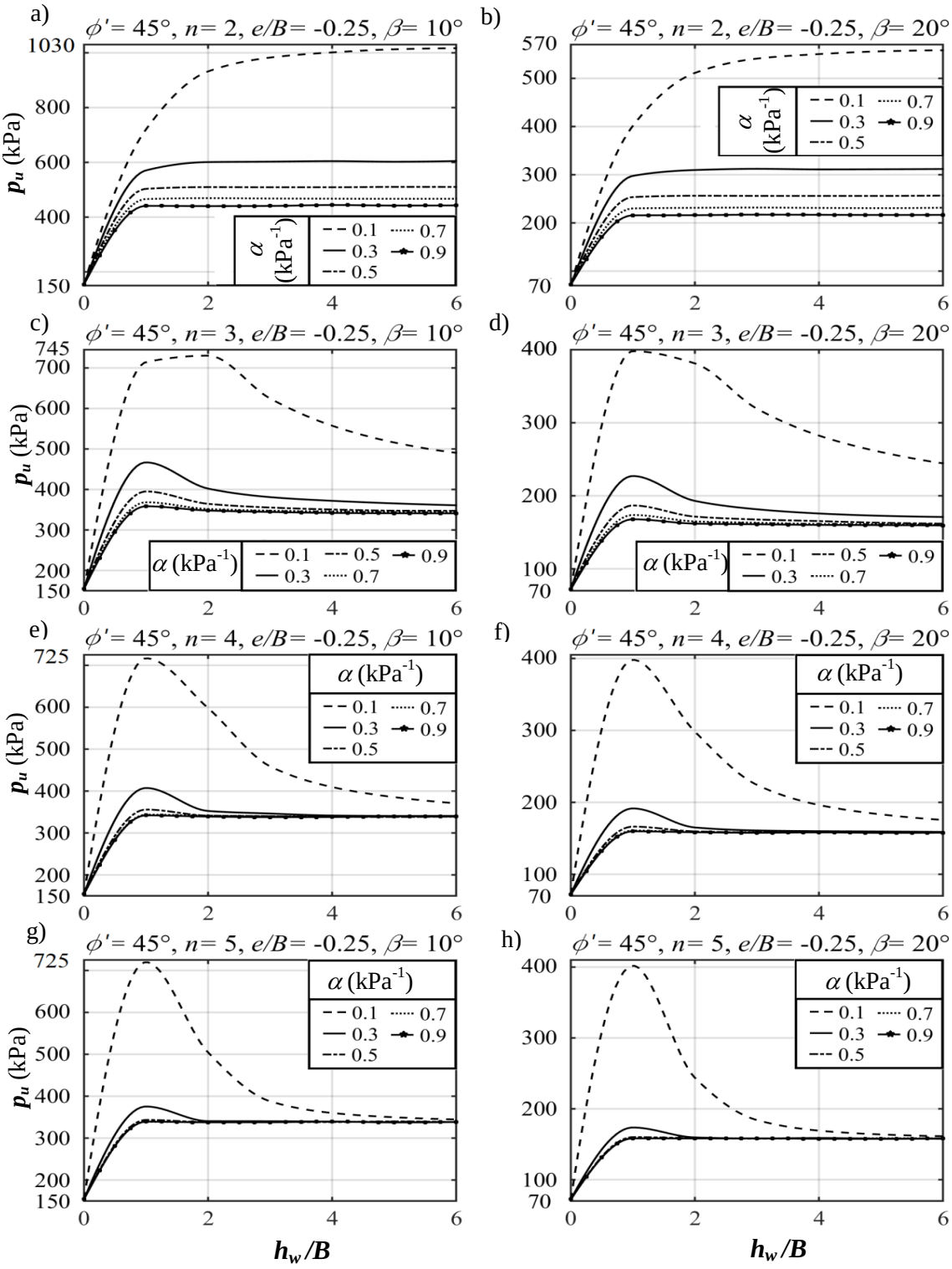

Figure 8.8 The variation of UBC (p_u) with respect to GWT for sands with ϕ' = 45°, e/B = – 0.25 and subjected to two β, namely, (a,c,e,g) β=10°; (b, d, f, h) β=20°; and corresponding to four values of n, namely, (a,b) n =2; (c,d) n =3; (e,f) n =4; and (g,h) n =5.

suction stress in the unsaturated medium gives rise to the internal power dissipation.

b) With the lowering of the water table, the p_u of any arbitrary soil subjected to a certain loading condition increases and attains either a horizontal plateau (for well graded soils) or a pronounced peak point (for uniformly graded soils). The water table position at which the bearing capacity is maximum is denoted here as $h_{w,opt}/B$. The presence of $h_{w,opt}/B$ is also reported by Vahedifard and Robinson (2016) and Du et al. (2021) for strip footing on unsaturated soils experiencing vertical and concentric loading. Beyond $h_{w,opt}/B$, the curves representing high n soils, decrease at a considerable rate and approaches to a constant value. This decrement rate lowers down with the increase in n and α.

c) For relatively low α's, the rate of improvement of p_u is notably higher and the $h_{w,opt}/B$ becomes more prominent. Furthermore, the occurrence of $h_{w,opt}/B$ becomes more pronounced and closer to the ground surface as the desaturation rate increases and the frictional strength decreases. Nevertheless, for lower n ($n \leq 2$), $h_{w,opt}/B$ does not exist within the considered vadose zone. Figure 8.9 presents the variation of p_u with respect to the GWT position corresponding to three different loading position (e/B=0.25, 0.0, and –0.25) and two n values, namely, n=1.2 and n=1.5. The lower value of n not only exhibits high p_u value but also shows a significant variation in the trend of the bearing capacity profiles. No matter whatsoever be the loading position, the bearing capacity continuously increases for n=1.2 but approaches towards a horizontal plateau for n=1.5.

d) Irrespective of the loading configuration and the soil strength, the bearing capacity profile representing α =0.1 remain quite distinct and significantly

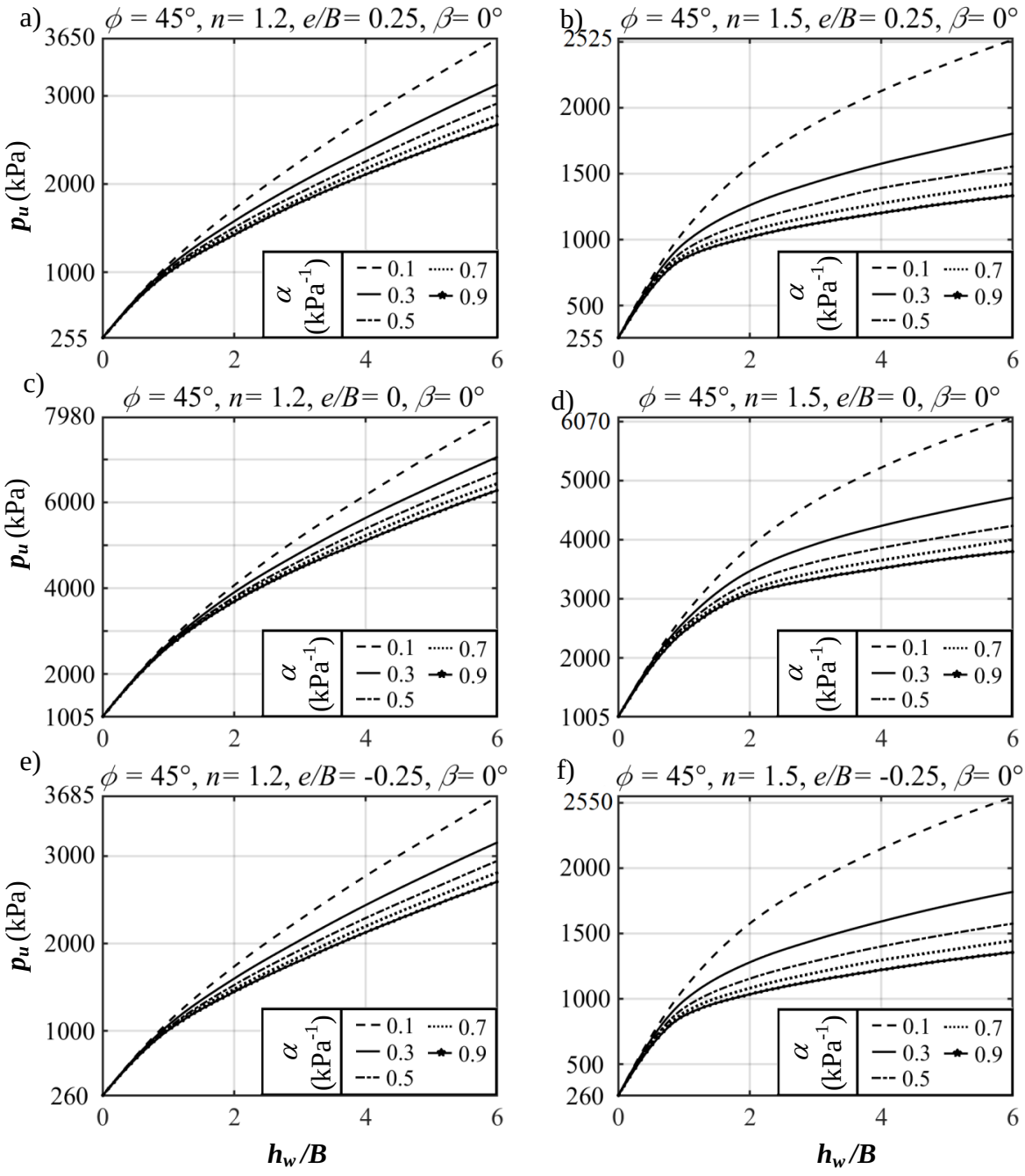

Figure 8.9 The variation of p_u with respect to GWT for sands with ϕ' = 45° and corresponding to (a) n =1.2, e/B=0.25; (b) n =1.5, e/B=0.25; (c) n =1.2, e/B=0; (d) n =1.5, e/B=0; (e) n =1.2, e/B=–0.25; and (f) n =1.5, e/B= – 0.25.

above the curves emerged from the other considered α. The enhancement in the load-withstanding capacity for α =0.1 can be attributed to the generation of relatively high matric suction as shown in Figure 7.3. The curves corresponding

to $\alpha \geq 0.3$ remains separated within a very narrow band, and for higher n they overlap over each other after a certain h_w. It can be inferred that the impact of the α parameter on the load-carrying capacity diminishes if the pore-size distribution of the soil becomes narrow and the water table is at appreciable distance beneath the ground surface. This observation is in well accordance with the suction stress profiles as depicted in Figure 7.3.

e) Compare to its vertical counterpart, the inclined load reduces load-bearing capacity of the strip footing to a significant extent. However, the trend of this reduction with respect to the load inclination is nonlinear. For instance, the percentage reduction of p_u for a strip foundation rested over a 35° soil with n=3, α=0.1, h_w/B= 6, and e/B=0 is 40.7% and 47.6% when the load angle (β) changes from 0° to 10° and 10° to 20°, respectively. There is a minute shift of $h_{w,opt}/B$ towards the ground surface as the load inclination increases.

f) By examining the curves, it can be further observed that the reduction of p_u due to the effect of load inclination are unaffected by the air entry values but gets influenced by the pore spectrum number. The percentage reduction of p_u is higher for the soils with low n value.

g) Not only the load inclination, but the position of the applied load over the footing also makes a huge influence on the estimated load bearing capacity. As the eccentricity of the load increases in either side, there is a significant decrement in p_u. If the eccentric load is vertically directed, no matter whichever side of the central axis the load is being placed, the bearing capacity will remain to be the same. But if the load is making a certain angle, the positive and the negative eccentricity, as shown in Figure 8.1, change the direction of the loading with respect to the footing central axis; positive eccentricity indicates reinforced

condition and the negative eccentricity denotes partially compensated condition. Table 8.1 presents the variation of UBC for the two *e/B*'s (0.25 and –0.25) corresponding to various combinations of α, β, *n* and ϕ. Irrespective of the soil parameters and loading direction, the UBC for *e/B* = 0.25 is greater than that of *e/B* = –0.25. The percentage-wise differences are also tabulated. It can be clearly viewed that this difference enhances with the increase in α, β, *n*, and ϕ.

Table 8.1. A comparative study of UBC to check the effect of three combinations of concentric/eccentric and vertical/inclined loading on strip foundation rested over unsaturated sands (ϕ = 35°) with various α and *n* values and fluctuating GWT.

van-Ganuchten's parameters	h_w/B	*e/B*=0	*e/B* =0.25	%	*e/B* =0	%
		β=0°	β=0°		β=10°	
α=0.1, *n* =2	1	519.97	210.74	59.44	321.61	38.15
	2	693.33	269.16	61.18	420.74	39.32
	3	740.3	284.01	61.64	447.22	39.59
	4	756.07	289.21	61.75	454.98	39.82
α=0.5, *n* =2	1	453.41	135.13	70.20	248.26	45.25
	2	498.7	136.69	72.59	253.08	49.25
	3	501.6	136.79	72.73	253.6	49.44
	4	502.09	136.83	72.75	253.53	49.51
α=0.1, *n* =4	1	518.54	209.01	59.69	321.36	38.03
	2	518.5	159.22	69.29	297.71	42.58
	3	412.03	119.27	71.05	297.71	27.75
	4	375	104.27	72.19	211.63	43.57
α=0.5, *n* =4	1	336.36	85.91	74.46	190.16	43.47
	2	321.83	82.12	74.48	181.55	43.59
	3	320	81.48	74.54	180.68	43.54
	4	320.07	81.47	74.55	180.74	43.53

h) Table 8.2 further depicts the variation of the UBC of the strip footing subjected to (a) vertical and eccentric loading (e/B =0.25 and β=0°), and (b) concentric and inclined loading (e/B =0 and β=10°). Four different combinations of α and n are taken for the comparisons. It appears that irrespective of the SWRC model parameters, eccentricity reduces the UBC more than the load inclination. Higher the α value higher is the percentage reduction of UBC; however, the role of α gets suppressed with the uniformity of the pore structure. Moreover, the percentage reduction of the UBC is predominant when the GWT fluctuates near the ground surface.

Table 8.2. The variation of p_u for positive and negative eccentricity corresponding to various hydromechanical properties of soil.

β	α	ϕ	n =2			n =4		
			e/B		% decrease	e/B		% decrease
			0.25	-0.25		0.25	-0.25	
10°	0.1	35°	220.13	196.75	-10.62	131.89	106.17	-19.51
		45°	859.79	731.97	-14.87	819.06	597.96	-26.99
	0.5	35°	112.99	91.21	-19.27	68.63	50.47	-26.46
		45°	695.68	509.62	-26.75	501.03	341.32	-31.88
20°	0.1	35°	132.92	119.78	-9.88	75.56	57.34	-24.12
		45°	624.38	511.21	-18.13	441.15	298.25	-32.39
	0.5	35°	65.09	49.31	-24.25	38.56	23.77	-38.34
		45°	375.78	256.32	-31.79	273.89	159.59	-41.73

8.4.2 Normalized V-H failure envelopes

Figure 8.10 shows the interaction diagram in V/V_{max}– H/V_{max} plane for ϕ' = 35° soil, α = 0.1, 0.5 kPa^{-1} and different value of h_w and n; (a) V and H are the vertical and horizontal components of total load, and (b) V_{max} represents the maximum load the strip footing can withstand when placed over the same unsaturated sand. Needless to say, the maximum load is noted when the applied load is vertical and concentric. It can be well

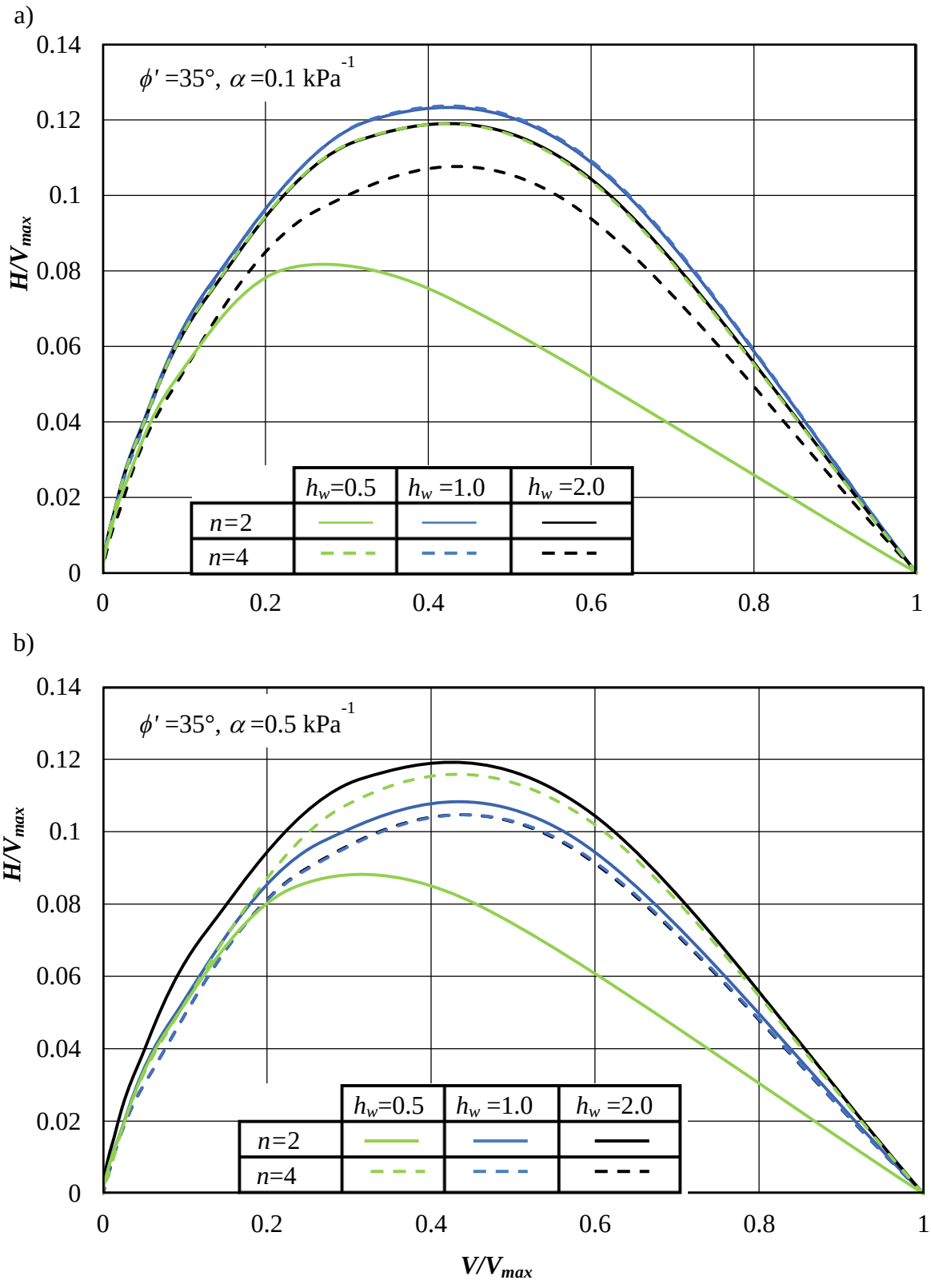

Figure 8.10 Interaction diagram in the $V/V_{max} - H/V_{max}$ plane for ϕ' =35°, α =0.1, 0.5 kPa^{-1} and different value of h_w and n.

observed that the size and the shape of the normalized *V–H* envelopes depend highly on the unsaturated soil properties and the GWT position. The effect of the soil gradation on the *V-H* cross-section appears to be quite dominating when the GWT lies near the ground surface (h_w/B =0.5). Except the curves corresponding to h_w/B =0.5 and n =2, the peak point (i.e. maximum value of horizontal force, H_{max}) of all other curves are higher for α =0.1 kPa^{-1} and occurs within the range of V/V_{max} equals to 0.40 to 0.45. The numerical values of H_{max} for these cases falls in the range of 0.107–0.123V_{max}; indicating that the inclination angle pertaining to the occurrence of the peak point on the *V–H* failure envelopes is relatively higher for the variably saturated soil than the fully saturated one.

Figure 8.11 further illustrates the effect of α on the normalized *V–H* envelopes corresponding to various positions of the groundwater table. The interaction diagram in V/V_{max}– H/V_{max} plane is plotted for the soil having ϕ'=30°, and n=4. The solid lines pertain to α=0.1 kPa^{-1} and the dashed line represents the curves for α=0.5 kPa^{-1}. The profiles corresponding to higher α is positioned at a relatively lower elevation. The deviations between the profiles of two α's become significantly high for h_w/B=2 but almost negligible for h_w/B=1. This may be attributed to the fact that h_w/B=1 corresponds to the critical water table position for both the chosen α of the concerned soil.

8.4.3 Nodal Velocity Patterns

The nodal velocity contours are drawn to represent the magnitude and the direction of soil particles movement at various nodal points within the considered soil domain. Figures 8.12–8.15 depict the nodal velocity patterns corresponding to various loading configurations and unsaturated soil properties. A curvilinear influential zone, encompassing the footing, is developed, in which the absolute magnitudes of the nodal

velocities become significantly higher than the rest part of the soil domain; this region is termed as the *zone of influence*, (Z_{inf}).

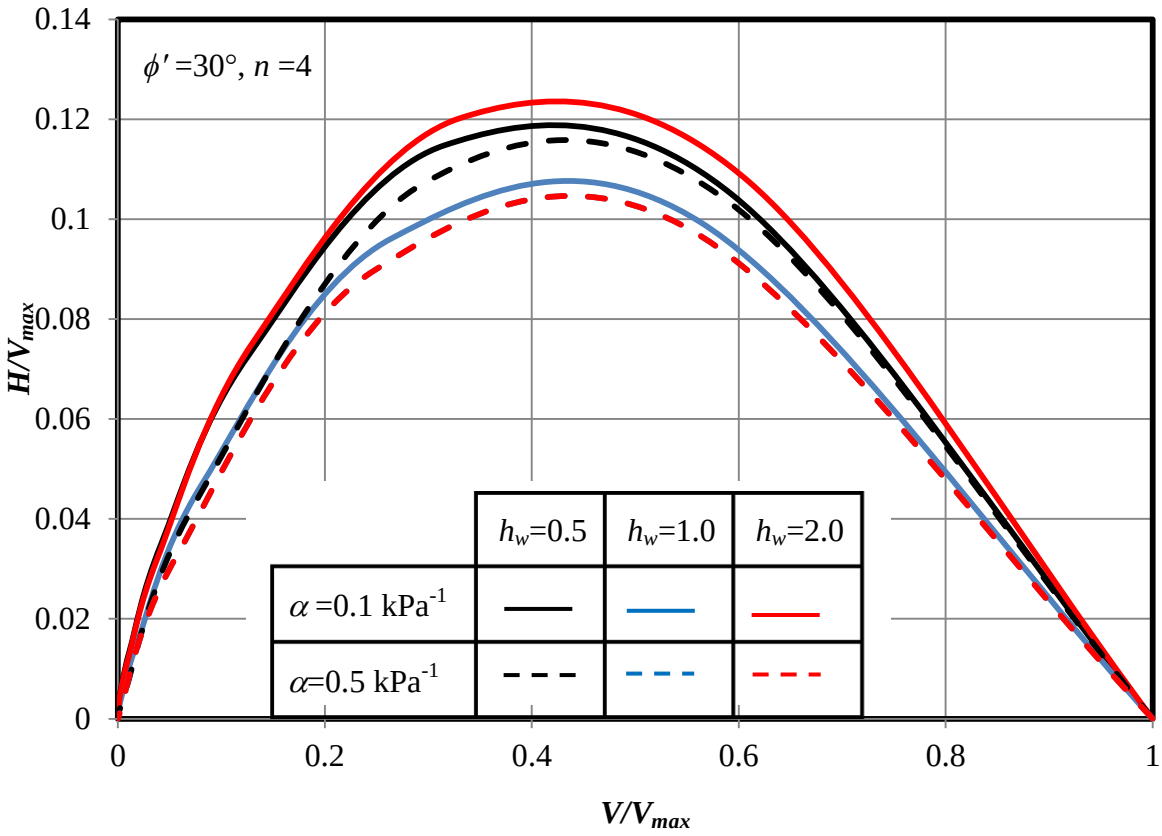

Figure 8.11 Interaction diagram in the $V/V_{max} - H/V_{max}$ plane for and different value of h_w and α.

Irrespective of the chosen input parameters, the following two observations are made: (a) the magnitudes of the velocities along the ground surface near the footing edge become significantly higher than the velocities of the soil mass just beneath the footing base, and (b) the velocity discontinuities are mainly effective only near the footing edge and these discontinuities gradually diminish continuously away from the footing edge.

Figure 8.12 represents the nodal velocity pattern for strip footing rested on unsaturated sandy stratum with ϕ'=35°, h_w/B=1, n=4, α = 0.3 kPa^{-1}, and subjected to

different loading position and orientation; Figures 8.12a, 8.12c, and 8.12e depict the velocity contour for concentric loading and Figures 8.12, 8.12d, and 8.12f correspond to the case where load is being applied eccentrically (e/B=0.25). The figure also shows the variation of Z_{inf} for vertical loading (Figures 8.12a and 8.12b) as well as two different inclined loading, namely, β=10° (Figures 8.12c and 8.12d) and β =20° (Figures 8.12e and 8.12f). The Z_{inf} appears to be symmetric when the external load is applied vertically at the centre of the foundation. Asymmetric velocity contour is manifested by eccentric and/or inclined loadings. Irrespective of the loading type and the soil properties, the resultant velocities near the footing edge appear to be the maximum and it gradually reduces along the ground surface. While the load is eccentrically placed over the footing, the velocity vector is appreciably higher near the footing edge of the loading side. On the other half of the footing (no-loading side), the magnitude of the velocity vector is significantly less. The nodal velocity contour gets tremendously influenced by the load inclination. Figures 8.12c and 8.12e depicts that the inclined load applied at the center position of the footing restrict Z_{inf} solely on one side of the footing. The asymmetricity nature of Z_{inf} is more pronounced for inclined and concentric loading (ICL) rather than vertical and eccentric loading (VEL). Load eccentricity enforces the velocity vectors to be concentrated near the loading side and load inclination pushes the velocity vectors on the loading direction and thus eventually results in small volume of overall failure domain. Nevertheless, the vertical extent of Z_{inf} seems to be higher for the ICL; this indicates that, unlike the VEL, the maximum suction stress zone is encompassed within the failure surface generated from ICL. This is why the UBC of ICL is higher than that of VEL. Figures 8.12d and 8.12f display the combined effect of load eccentricity and inclination on the magnitude and overall extent of velocity contours. The velocity vectors corresponding to VEL remain consistently vertically

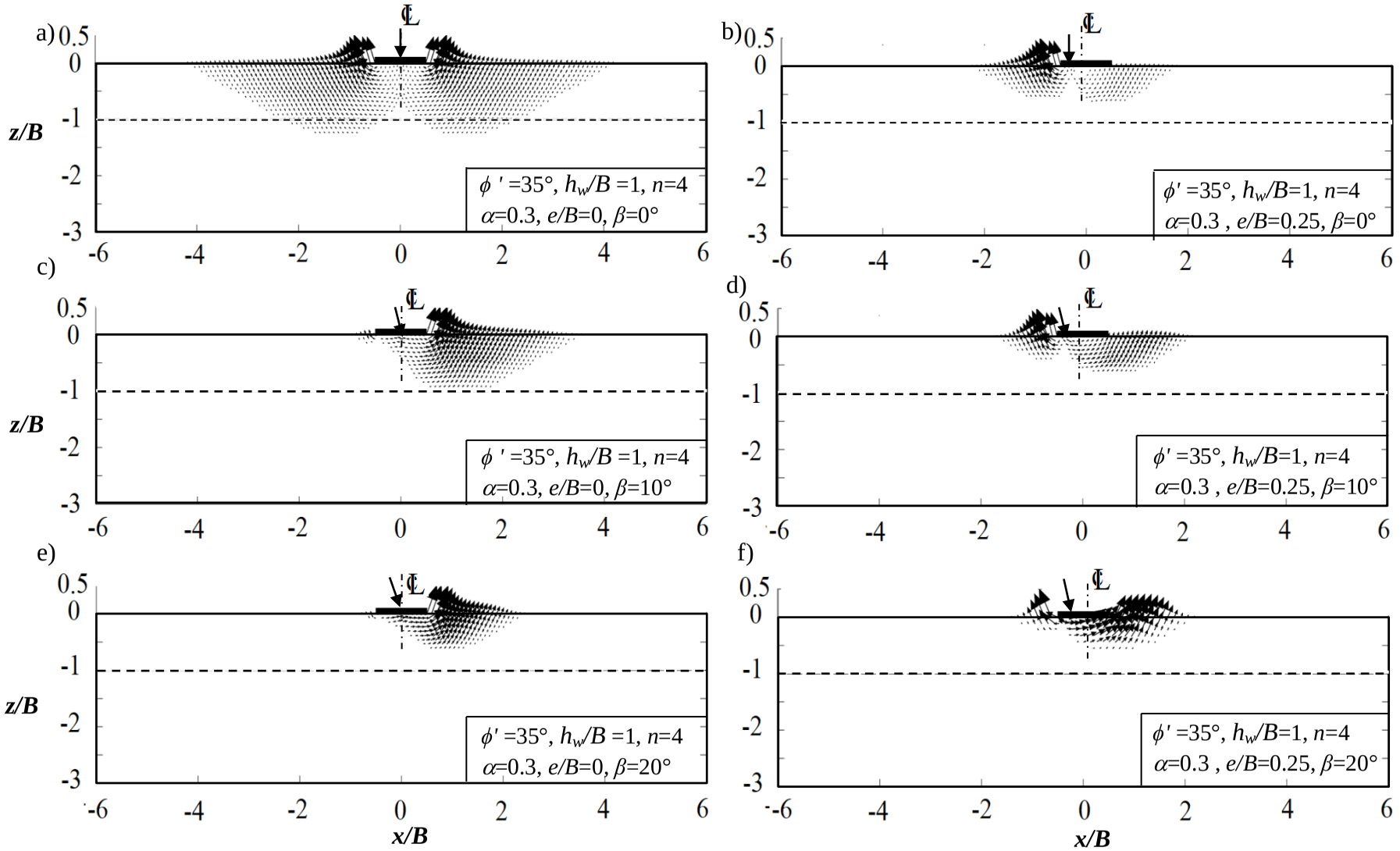

Figure 8.12 Nodal velocity pattern for strip footing on sandy soil (ϕ' = 35°) for different e and β values: a) e/B = 0, β=0°; b) e/B = 0, β=10°; c) e/B = 0, β=20°; d) e/B = 0.25, β=0°; e) e/B = 0.25, β=10°; f) e/B = 0.25, β=20°.

downwards to some distance below the footing base beneath the loading position. Unlike the vertical loading, the velocity vectors below the footing base subjected to inclined loading become immediately inclined foundation subjected to inclined loading are directed horizontally/ obliquely. The rigid triangular wedge beneath the foundation is not being created for the inclined loading; it appears that the failure is no longer govern by the bearing capacity mechanism rather it is due to the direct sliding along the interface. With the increase in load inclination, the magnitude of the velocity vectors, especially near the ground surface, enhances appreciably; nevertheless, the horizontal and the vertical extent of the influence zone reduce to a great extent. It can be summarized that deviating the central position and disrupting the verticality of the applied load narrows down the volume of the soil encompassed within Z_{inf} considerably.

The impact of α on the velocity contour is depicted in Figure 8.13. Three α's, namely, α=0.1, 0.3, 0.5 kPa^{-1} are chosen for showing the comparison. The rest of the input parameters concerning the material model (ϕ' =45°, n =4), loading arrangement (e/B=0.25, β =0°), and GWT position (h_w/B=1) are kept to be the same. With the increase in α, (a) there is a curtailment in the size of the overall influence zone, (b) the concentration of the velocity vectors and the velocity discontinuities near the footing edge of the loading side narrows down, and (c) the magnitude of the velocity vector decreases. However, in contrast to the loading region, the horizontal extent of the velocity contour on the non-loading side relatively decreases with the expansion in the boundary effect zone. It can be interpreted that the point and orientation of load application significantly impacts those sands having relatively lower AVE.

Figure 8.14 illustrate the effect of n on the nodal velocity vector of strip footing rested on partially saturated soil (ϕ' = 45°, h_w/B=2, α = 0.1 kPa^{-1}) and subjected to vertical eccentric loading (e =0.25B). The figures are plotted for two n values, namely,

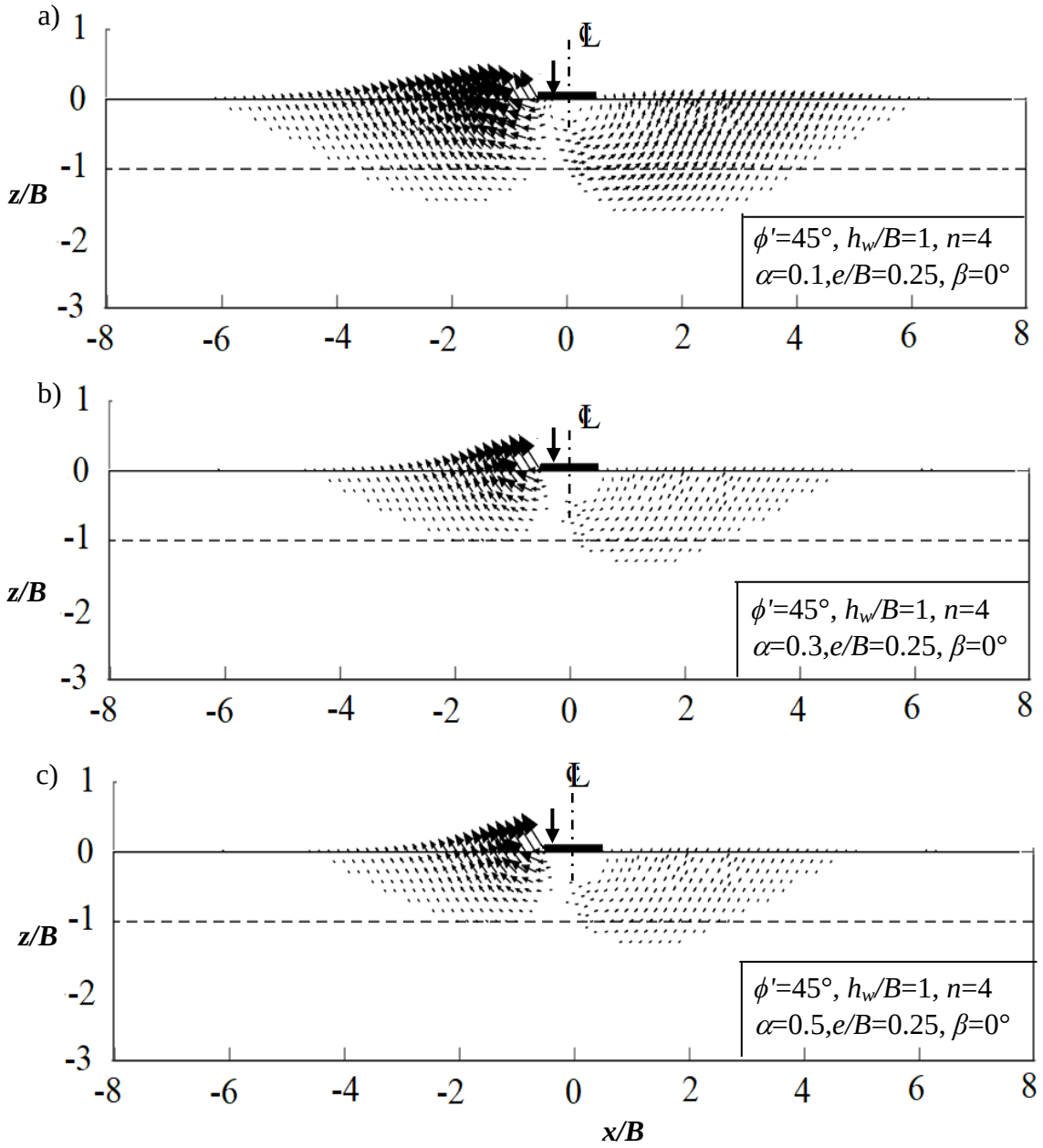

Figure 8.13. Nodal velocity pattern for strip footing subjected to vertical and eccentric loading and the supporting unsaturated sand having ϕ' = 45° and different α: a) α = 0.1; b) α = 0.3; c) α =0.5.

n =2 and n = 4. The manifestation in velocity contour due to the increase in n is qualitatively the same as observed previously for increasing α. As the gradation of the sands approaches uniformity, the suction stress decreases and results in smaller failure zone with lower magnitude of velocity vectors.

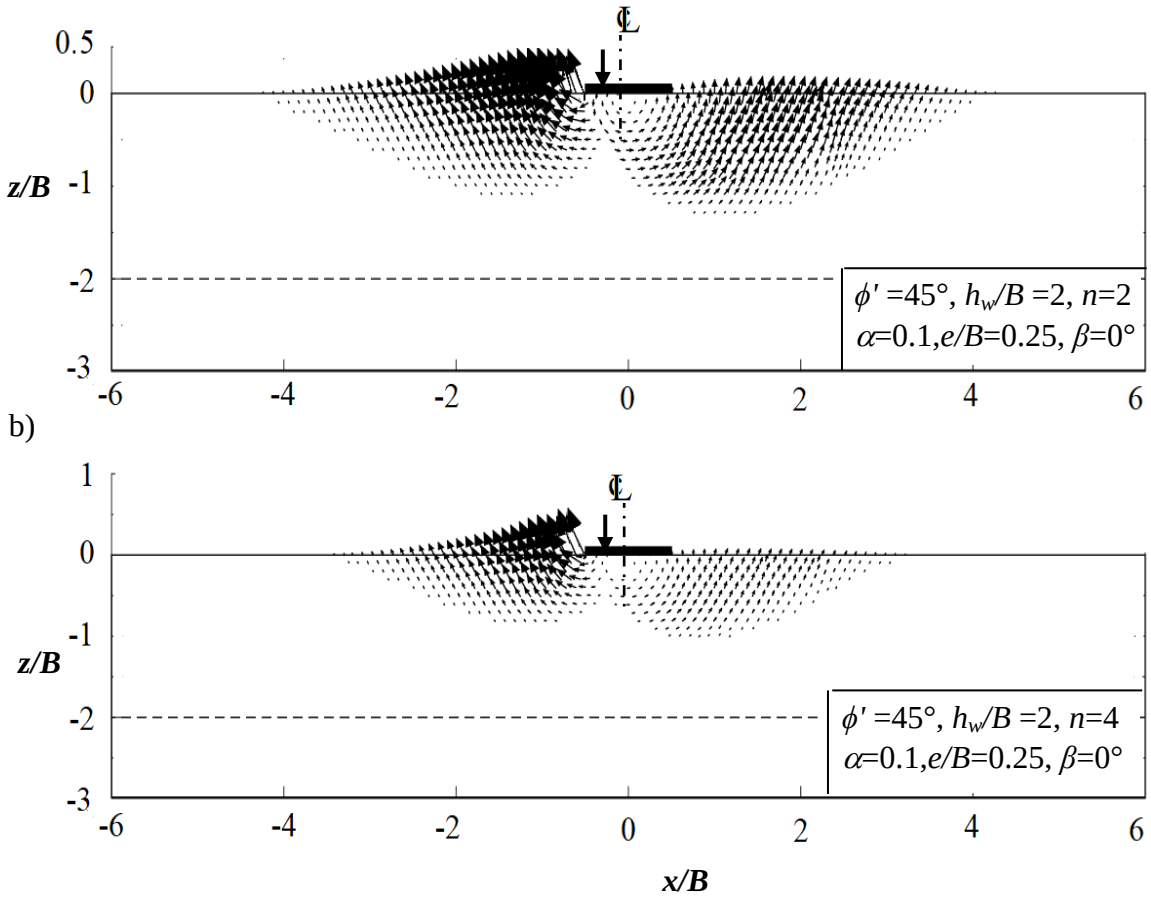

Figure 8.14 Nodal velocity pattern for strip footing subjected to vertical and eccentric loading and the supporting unsaturated sand having ϕ' = 45° with two n values: a) n = 2; and b) n= 4.

The effect of internal friction angle (ϕ') on the extent and form of the failure zone is displayed in Figure 8.15. The chosen soil properties are: h_w/B=1, n=4, α=0.1 kPa^{-1}, e =0.25B, β =0°. The analyses are carried out for two ϕ's: 35° and 45°. With the increase in ϕ, the magnitude of the relative velocity vector enhances and there is a tremendous growth in the size of Z_{inf}.

Figure 8.16 further illustrates the effect of GWT position on the velocity contour that develops beneath the strip footing resting on unsaturated sands (ϕ = 45°, n = 4, and α = 0.1 kPa^{-1}) and subjected to vertical concentric loading. It can be seen that with the lowering of water table surface, the size of the Z_{inf} gets compressed, the magnitude of velocity vector gets enhanced, and the triangular elastic rigid block gradually attenuates.

The soil movement beneath the central portion of the footing becomes practically negligible.

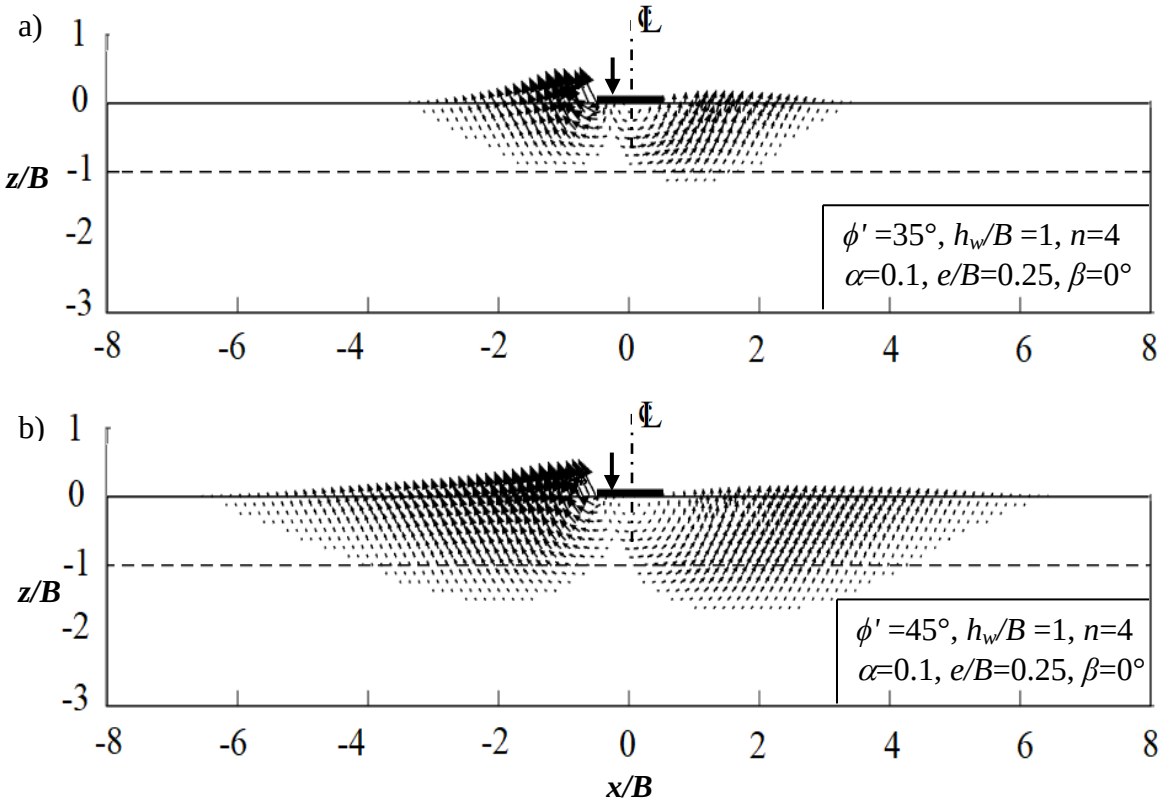

Figure 8.15. Nodal velocity pattern for strip footing subjected to vertical and eccentric loading and the supporting sand having different ϕ' : a) ϕ' = 35°; b) ϕ' = 45°.

8.5 COMPARISONS OF RESULTS

Table 8.3 presents the comparison of the obtained upper bound solutions with the results provided by (i) analytical method (Hansen, 1970; Vesic, 1973), (ii) finite element (FE) method (Loukidis et al., 2008), (iii) laboratory model tests (Patra et al., 2012), and (iv) regression analysis (Ganesh et al., 2017) performed on the available laboratory model test results. The comparison is made on the non-dimensional reduction factor (RF) which is defined as the ratio of bearing capacity of strip footing with eccentric and/or oblique load to the bearing capacity of strip footing with concentric

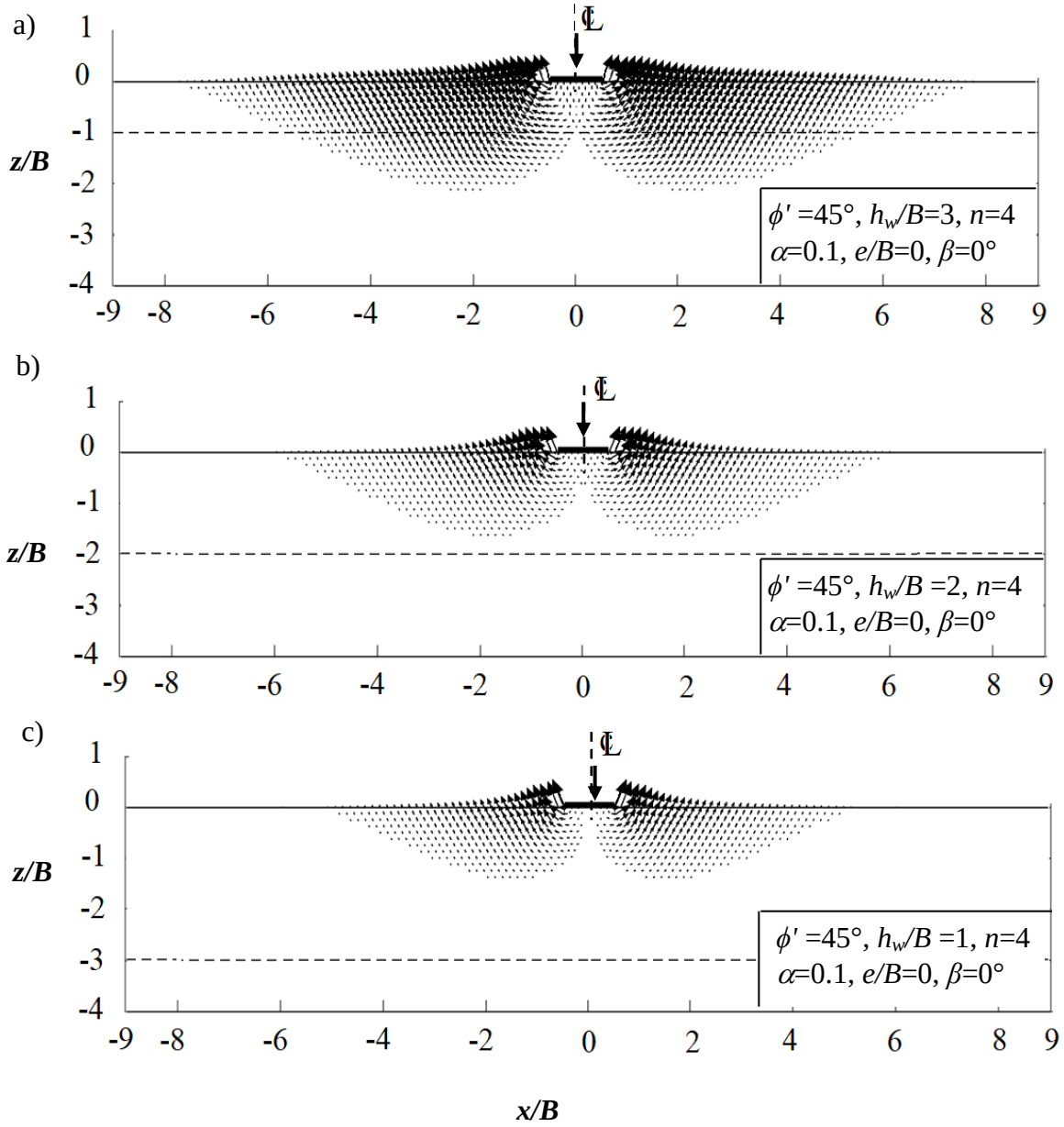

Figure 8.16 The nodal velocity pattern for strip footing subjected to vertical and concentric loading and the supporting sands (ϕ' = 45°) having different GWT position: a) h_w/B = 3; b) h_w/B = 2; c) h_w/B =1.

vertical load. The RF explicitly gives an impression that to what extent the bearing capacity gets impacted due to the shifting of the load (from the footing axis) and disrupting the verticality of the load.

This comparison is carried out on the saturated sands. The present results are in well accordance with the analytical and FE solutions. Irrespective of the loading positi-

Table 8.3. A Comparison of reduction factor (RF) values for strip footing resting on sandy soil subjected to combined loading.

β/ϕ'	e/B	Present study[a]	Hansen (1970)[b]	Vesic (1973)[b]	Loukidis et al. (2008)[c]	Patra et al. (2012)[d]	Ganesh et al. (2017)[e]
1/3	0	0.497	0.516	0.553	0.553	0.436	0.441
	0.1	0.351	0.329	0.354	0.409	0.349	0.282
	0.2	0.198	0.184	0.200	0.230	0.261	0.155
	0.3	0.088	0.080	0.087	0.091	0.173	0.070
	0.4	0.022	0.017	0.017	0.019	0.081	0.016

Note:a: The solutions are obtained on the basis of finite element upper bound with the help of exterior point method.
b: The solutions are obtained on the basis of analytical method.
c: The solutions are obtained on the basis of finite element method
d: The solutions are obtained on the basis of the experimental results
e: The solutions are obtained on the basis of regression analysis of the laboratory model test results

ons, the present numerical values are on the higher side than the results reported from the regression studies which are based on 254 experimental test data. This can be attributed to the upper bound nature of the present problem.

The validation regarding bearing capacity of strip footing on unsaturated sandy soil is well discussed in Section 7.5.4. The findings obtained in this study align with the results found in existing literature

8.6 SUMMARY

By using finite element upper bound theorem, the present chapter obtains the ultimate load bearing capacity of the strip foundation rested over the unsaturated sands and subjected to eccentric and/or oblique loading. The form of the constraints remains to be the same as that of the saturated formulation; however, the power dissipation terms in the objective function get modified due to the additional incorporation of the suction stress. The suction stress is spatially obtained by considering vG SWRC model,

Darcian flow law, Gardner's hydraulic conductivity function, and vG-Mualem's prescription on the asymmetry parameter of the SWRC curve. The soil medium above the water table is modelled with the aid of suction stress-dependent extended Mohr-Coulomb yield criterion. A rigorous investigation is carried out and a series of bearing capacity charts are prepared for viewing the effects of water-table fluctuations, flow conditions, hydromechanical soil properties, loading direction and its application point. It is well observed that if the load is being placed anywhere but along the central axis of the footing, the bearing capacity reduces significantly. There is a certain position of groundwater table surface, especially, for the sands having a larger capillary saturation zone, at which the load withstand capacity of the soil becomes maximum. The design charts prepared in this article will be helpful for the practicing engineers dealing with the eccentric and/or inclined loading. The nodal velocity contours drawn for few specific cases are quite insightful and provides a clear impression of the variation of the velocity vectors and the extent of the failure zone.